nature geoscience

Article https://doi.org/10.1038/s41561-023-01320-1

Southeast Asian ecological dependency on Tibetan Plateau streamflow over the last millennium

In the format provided by the authors and unedited

Supporting Online Material for

Southeast Asian ecological dependency on Tibetan Plateau streamflow over the last millennia

Materials and methods

Tree-ring data. During the 2007–2018 field seasons, we collected increment cores from juniper (*Sabina tibetica*) and spruce (*Picea likiangensis*), and fir (*Abies forrestii*) from nine sampling sites in the southern Tibetan Plateau (Figure 1 and Supplementary Table 1). All sampling was conducted in open stands growing on thin or rocky soils. The harsh environment implies that the tree growth is moisture limited (Supplementary Figure 1). Usually, two cores were extracted from each tree using increment borers. An additional moisture-sensitive tree-ring width series for *Sabina tibetica* [3] was also used in this study.

The increment cores were dried, mounted, polished and the tree-ring widths measured to the nearest 0.001 mm. The cross-dated ring width series were verified using the COFECHA program [4]. Considering the low canopy density and limited tree-tree competition, we first used the ARSTAN program [5] to detrend the cross-dated ring width sequences using a negative exponential or linear regression growth trend curve. Core indices were computed as the ratio of measured ring width to the fitted growth curve, and were averaged together (biweight mean) to produce the site chronologies. No variance-stabilization was implemented within ARSTAN to adjust chronology variance for changing number of samples over time. To ensure a sufficient common signal within the chronologies, the site chronologies used in the streamflow reconstructions described below were truncated prior to the period when the expressed population signal (EPS) [6] was > 0.85.

Streamflow data. Hydrological stations across the major transboundary river basins in Southeast and South Asia are relatively sparse and have missing data, and most of the hydrological stations on the southern Tibetan Plateau were installed after the 1950s. Monthly streamflow data from the Chiang Saen, Daojieba and Nuxia stations were obtained for the Mekong, Salween and Yarlung Tsangpo (the upper Brahmaputra) river catchments, which represent natural flows, covering the periods of 1957–2011, 1960–2007, and 1956–2004, respectively (Supplementary Table 1). We selected the instrumental streamflow data for the Mekong, Salween and Yarlung Tsangpo rivers for the streamflow reconstruction because they are the principal transboundary rivers in this region, and because the hydrological stations were located on the main channel and thus representative of streamflow variations over a large area. In the relatively uniform geographic environment of the southern Tibetan Plateau, the three rivers have similar seasonal and inter-annual variations (Supplementary Figure 2), which enabled us to reconstruct the water supply history of the Tibetan Plateau for Southeast and South Asia during the last millennium. Average annual streamflow of the three transboundary rivers is 1987×10^8 m^3, and the total June–September streamflow (1288.6×10^8 m^3) accounts for 65% of the annual runoff. The highest streamflow is in August, at 410.2×10^8 m^3, and the lowest is in February, at 42.6×10^8 m^3. Correlations of the sum of the annual streamflow measurements of all stations with the annual streamflow of the Mekong, Salween and Yarlung Tsangpo rivers computed over the 1960–2000 common period are 0.80, 0.74, and 0.78, respectively.

Characteristics of the streamflow reconstruction

The streamflow reconstruction accounts for 42.0–61.0% of the instrumental streamflow variance during the full calibration period of 1961–2004 CE. As shown in Supplementary Table

S2, all the results are statistically significant, and split-sample calibraton-validation statstics demonstrate the good predictive skill of the regression model.

The reconstructed and 30-year low-pass-filtered total September–July streamflow for the Mekong, Salween and Yarlung Tsangpo rivers are shown in Figure 1C. The reconstruction shows substantial low-frequency streamflow variability during the past 1000 years. The long-term mean of the streamflow reconstruction based on the regression models is 1576.5×10^8 for the period of 1000–2018 CE. The streamflow reconstruction indicates relatively high streamflow during the periods of 1000–1006, 1054–1197, 1235–1254, 1271–1281, 1340–1367, 1406–1422, 1512–1592, 1613–1625, 1678–1728, 1739–1753, 1773–1795, 1836–1871, 1892–1907, 1927–1966, and 1991–2018. In contrast, periods with low streamflow occurred during 1007–1053, 1198–1234, 1255–1270, 1282–1339, 1368–1405, 1423–1511, 1593–1612, 1626–1677, 1729–1738, 1754–1772, 1796–1835, 1872–1926, 1908–1928, and 1967–1990. As indicated by our streamflow reconstruction, 1054–1197 and 1423–1511 are respectively the longest periods of high and low streamflow since 1000 CE. Values beyond ±2 standard deviations (SD) indicate extremely dry and wet years, and on this basis 29 extremely dry years and 16 extremely wet years are identified. The most noteworthy feature in the late 20th century is the clear trend of increasing streamflow under global climatic warming, and 2000 and 2001 rank among the ten highest streamflow years. Our streamflow reconstruction is positively correlated with the instrumental sea-surface temperature (SST) fields of the North Atlantic and North Pacific Oceans during the instrumental period of 1961–2004 (Supplementary Figure 4)

The Community Earth System Model Last Millennium Ensemble (CESM-LME) simulation provides a long-term perspective for separating the roles of the two SST fields, due to its provision of all-forcing and individual-forcing simulations [9]. Based on the results of spatial correlation analyses with gridded runoff data [10] (Supplementary Figure 3, 4), we extracted the regional streamflow closely related to the reconstruction in the CESM-LME for comparison, and the inconsistent streamflow changes show the role of internal variability[11] (Supplementary Figure 5). The results also show that the AMV and PDO played specific roles in regional streamflow changes during the last millennium, by influencing the regional precipitation and temperature (Supplementary Figure 7-9). In the Current Warm Period (CWP) (1850–2005), all variables explain 88.0% of the decadal changes in regional streamflow, of which the most significant are ozone-aerosol and the AMV, which contribute 31.6% and 20.0%, respectively. In general, in the observations, the reconstruction, and the CESM-LME, internal variability (mainly the PDO and AMV) is the dominant factor influencing streamflow changes in the study region. However, during the CWP, the impact of intensifying human activities on streamflow changes cannot be ignored.

Under different emission conditions the runoff will continue to rise in the future. In the case of CESM-LME RCP8.5, the future period (2019–2100) has a runoff increase of 15.9% compared with the historical period (1850–2018), while in the four cases of CMIP6, it increased by 8.6% (SSP1-2.6), 11.1% (SSP2-4.5), 18.0% (SSP3-7.0), and 14.9% (SSP5-8.5), respectively (Supplementary Figure 9). In predictions it is estimated that radiative forcing by greenhouse gases and other factors will increase atmospheric humidity and significantly warm the Indian Ocean, supplying more water vapor to the study region [12, 13]. However, continuing emissions will lead to the reduction of the land-sea temperature gradient and the thermal difference, resulting in the weakening of monsoon circulation and precipitation, which may be why runoff in CESM-LME RCP8.5 and CMIP6 SSP5-8.5 is lower than in CMIP6 SSP3-7.0 [14,15]. However, the uncertainty regarding the hydroclimatic changes predicted by different models hinders the formulation of effective adaptation strategies. Although the multi-model ensemble (MME) method we used reduces the uncertainty to a certain extent, more model ensembles and downscaled climate hydrological data applicable to the region are still needed for prediction.

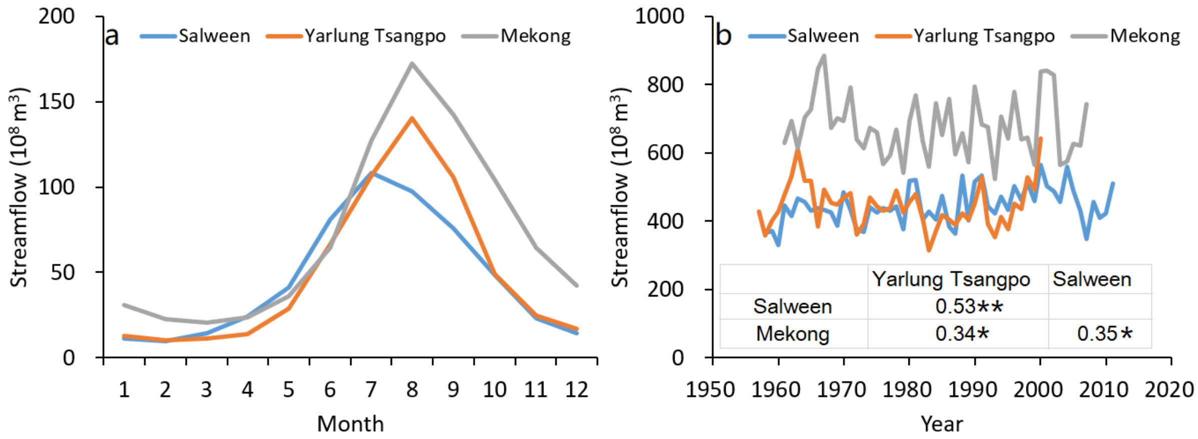

Supplementary Figure 1 (a) Monthly streamflow of the Mekong, Salween and Yarlung Tsangpo rivers. **(b)** Comparison of the annual streamflow of the Mekong, Salween and Yarlung Tsangpo rivers. Correlations among the annual streamflow of the Mekong, Salween and Yarlung Tsangpo rivers are showed. ** Significant at $p < 0.01$ (two tailed); * significant at $p < 0.05$ (two tailed).

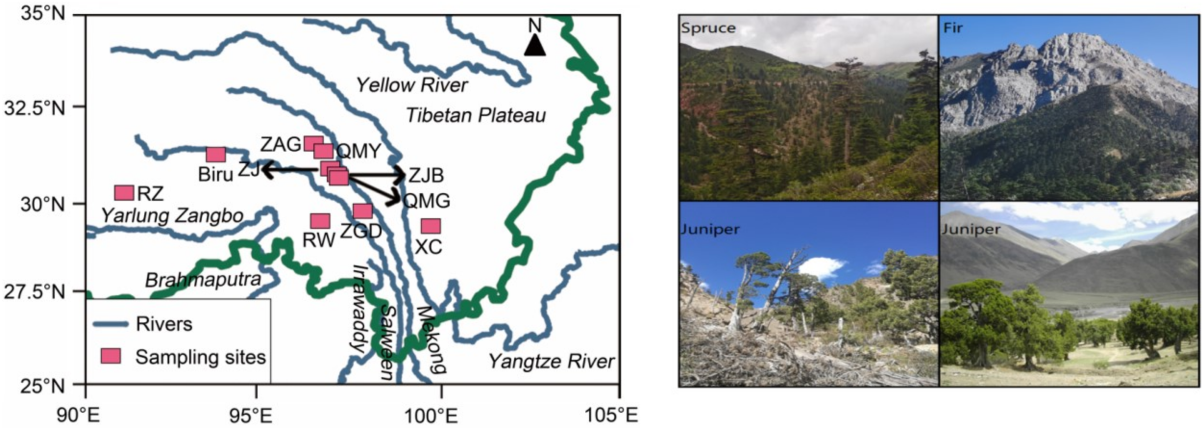

Supplementary Figure 2 Locations of tree-ring site. Examples of sampling sites within the southern Tibetan Plateau. The natural vegetation is open coniferous forest.

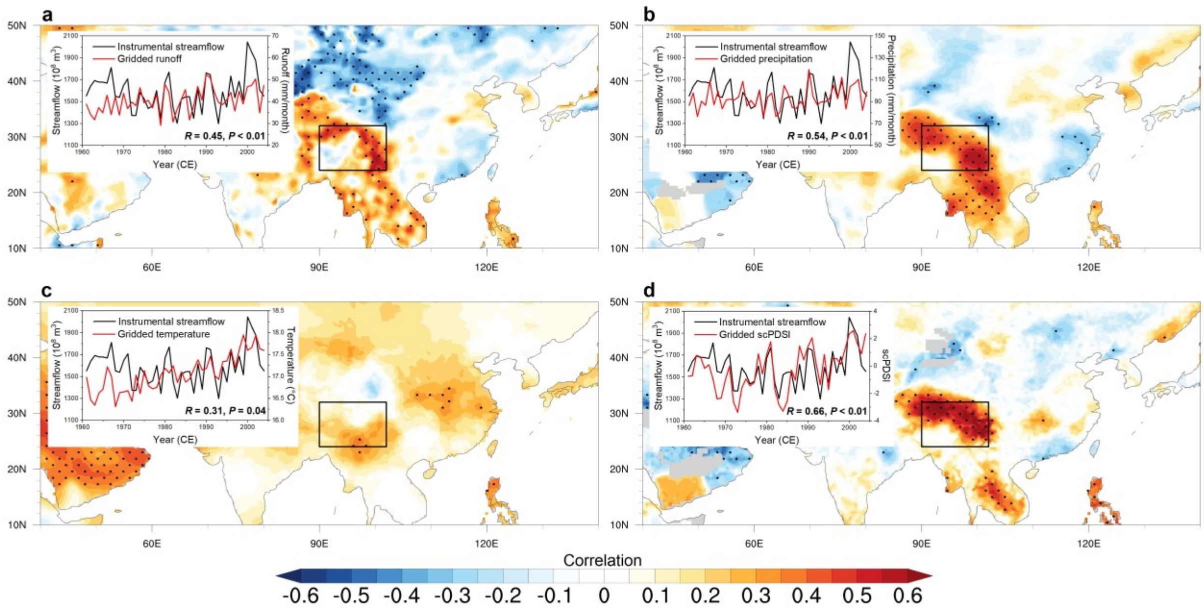

Supplementary Figure 3 Spatial correlation patterns of instrumental streamflow (September–July) with gridded streamflow **(a)**, precipitation **(b)**, minimum temperature **(c)**, and scPDSI **(d)** from 1961 to 2004. Dots indicate values above the 95% confidence level. The rectangle represents the area containing the sampling points, and the same below.

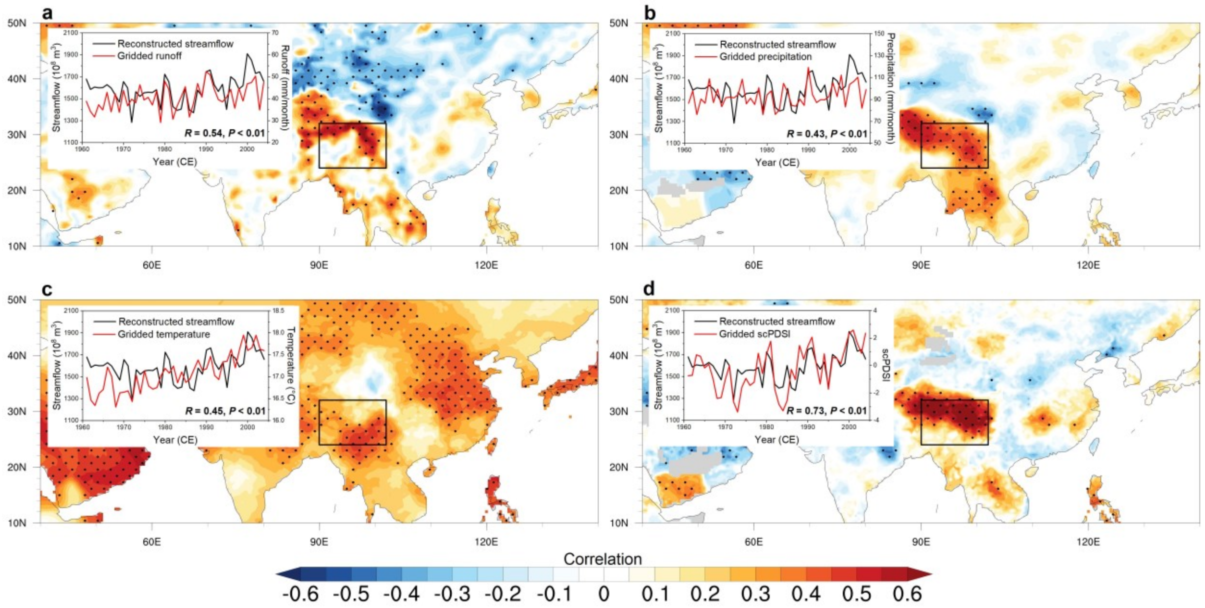

Supplementary Figure 4 Same as Fig. S3, but for the reconstructed streamflow based on tree rings.

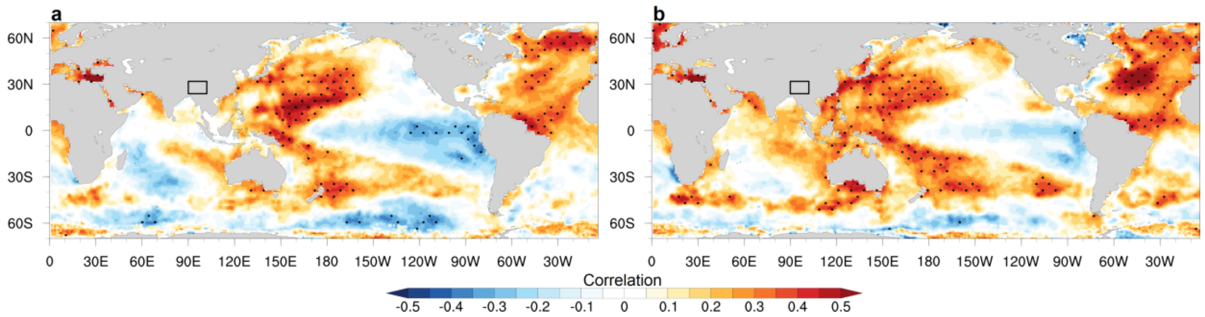

Supplementary Figure 5 Spatial correlation patterns of the instrumental **(a)** and reconstructed **(b)** streamflow with September–July SST from 1961 to 2004.

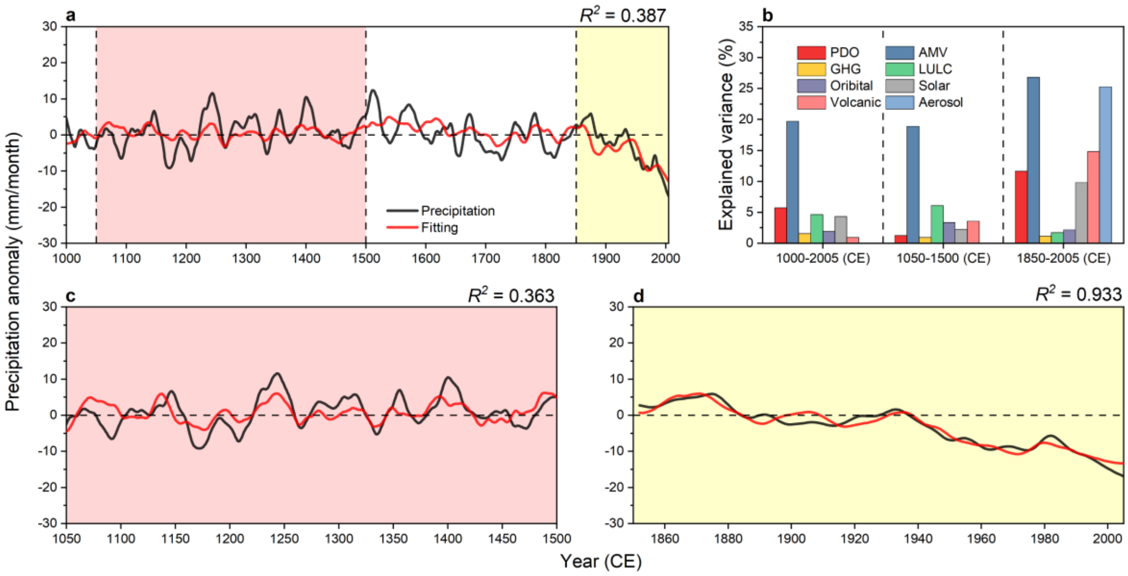

Supplementary Figure 6 (a) Regional precipitation changes attributed to the PDO, AMV, and external forcing by applying multiple linear regression (MLR) from 1000 to 2005 in the CESM-LME simulations. **(b)** Explained variance (%) of the streamflow changes in the CESM-LME simulations. **(c-d)** Same as **(a)**, but for different periods.

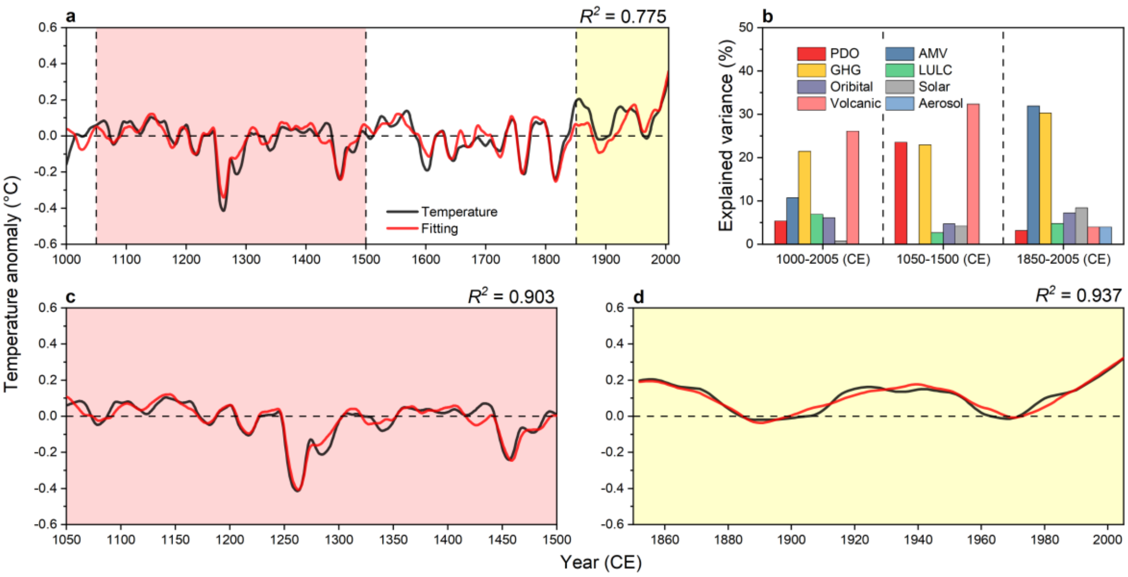

Supplementary Figure 7 Same as Fig. S6, but for the regional temperature changes in the CESM-LME simulations.

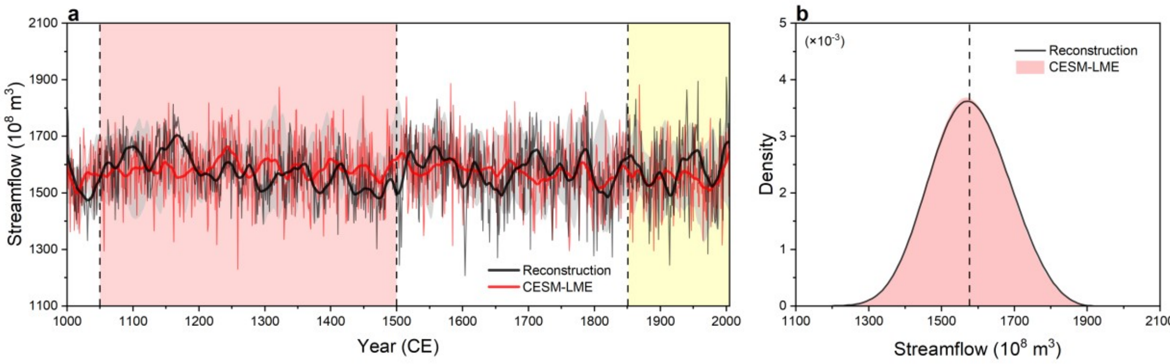

Supplementary Figure 8 Comparison of September–July streamflow from the reconstruction and CESM-LME. (**a**) The thin lines denote the original series, and the thick lines denote the results of 30-yr low-pass filtering. Shadings indicate the range of different members after smoothing. (**b**) Kernel probability density estimate for the simulated streamflow and the reconstructed streamflow.

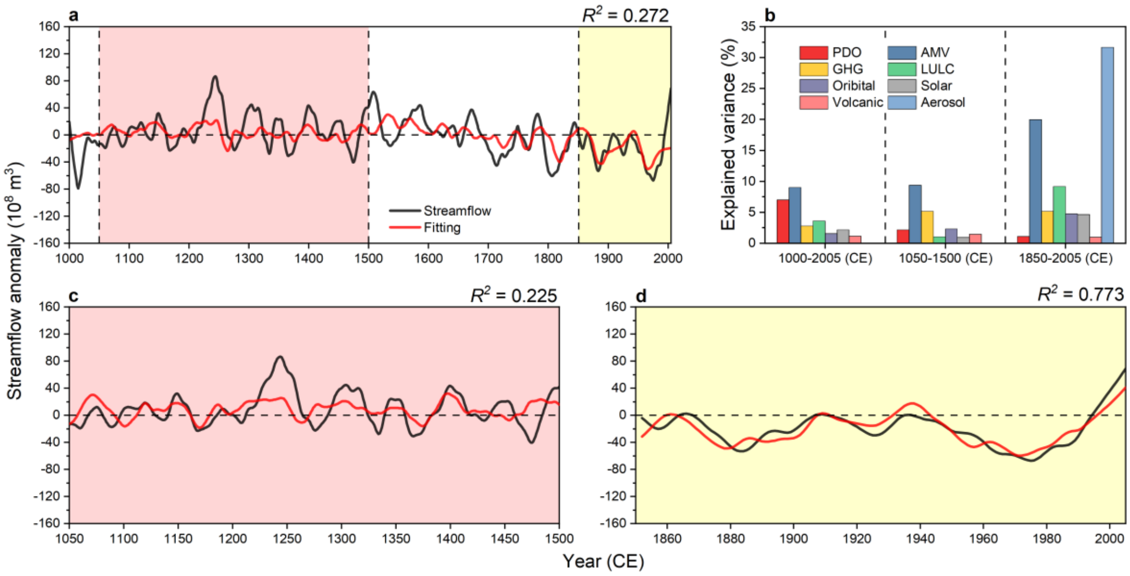

Supplementary Figure 9 Same as Fig. S6, but for the regional streamflow changes in the CESM-LME simulations.

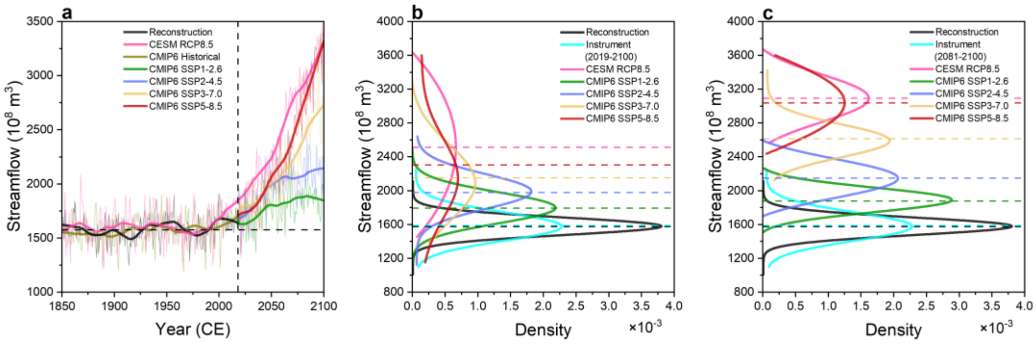

Supplementary Figure 10 (a) September–July streamflow changes under the reconstruction, CESM and different scenarios of CMIP6, from 1850 onwards. The thick lines represent 30-yr low-pass filtered curves and the horizontal dashed line represents the reconstruction mean. **(b)** Kernel probability density estimate of the regional streamflow in the reconstruction (1000–2018), the instrumental period (1961–2004), and the future (2019–2100), and their respective means (horizontal dashed lines). **(c)** Kernel probability density estimate of the regional streamflow in the reconstruction (1000–2018), the instrumental period (1961–2004), and in the future (2081–2100), and their respective means (horizontal dashed lines).

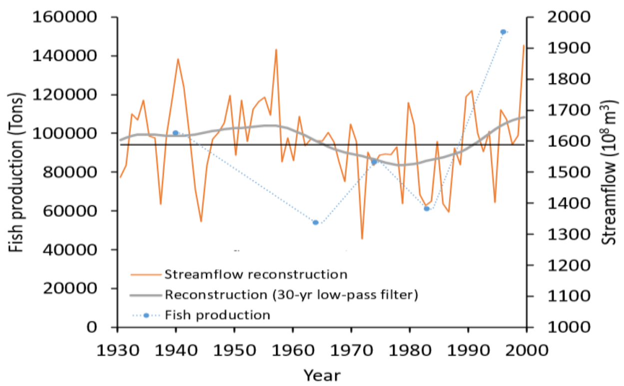

Supplementary Figure 11 Comparison between annual fishery catches of the Tonle Sap Great Lake [19] and the streamflow reconstruction

Supplementary Table 1 Site information and descriptive statistics for the tree-ring chronologies. Locations of the corresponding hydrological stations are shown in Fig. 1

Basin	Site	Lat. (N)	Long. (E)	Elevation (m)	Core/ Tree number	Length (EPS > 0.85)	Mean sensitivity	Standard deviation	Correlation with the streamflow reconstruction	Species
	XC [1]	29.13°	99.98°	3963	147/74	1520–2016	0.27	0.28	0.53	*Abies forrestii*
	QMG	31.07°	96.97°	4334	43/22	1500–2006	0.20	0.22	0.74	*Sabina tibetica*
	QMY	31.30°	96.57°	4370	143/72	1320–2020	0.13	0.19	0.68	*Picea likiangensis*
	RW	29.49°	96.77°	4005	163/82	1325–2018	0.01	0.13	0.40	*Picea likiangensis*
	RZ [2]	30.31°	91.51°	4238	180/90	1165–2018	0.27	0.29	0.43	*Sabina tibetica*
	ZAG	31.41°	96.46°	4388	48/24	1725–2006	0.13	0.19	0.59	*Sabina tibetica*
	ZGD	29.67°	97.92°	4301	37/20	1750–2013	0.48	0.45	0.48	*Sabina tibetica*
	ZJ	31.07°	96.97°	4295	94/47	1135–2020	0.17	0.22	0.51	*Picea likiangensis*
	ZJB	31.05°	96.99°	4334	74/37	1000–2020	0.16	0.19	0.82	*Sabina tibetica*
	Biru [3]	31.25°	94.25°	4230-4440	72/36	1080–2010			0.61	*Sabina tibetica*
Salween	Daojieba	24°59′	98°48′	685		1957–2011				
Mekong	Chiang Saen	30°19′	91°31′	358		1960–2008				
Yarlung Tsangpo	Nuxia	20°16′	100°05′	2910		1956–2004				

Note: MS is the mean sensitivity; SD is the standard deviation; EPS is the expressed population signal.

Supplementary Table 2 Calibration/verification statistics for the reconstructed September–July streamflow.

Reconstruction period	Calibration r^2	Verification r^2	Verification RE	Calibration period	Verification period	r^2
1000–1080	0.52	0.41	0.43	1983-2004	1961-1982	0.44
1080–1135	0.43	0.40	0.38	1983-2004	1961-1982	0.42
1135–1165	0.52	0.43	0.38	1983-2004	1961-1982	0.47
1165–1320	0.53	0.50	0.53	1983-2004	1961-1982	0.49
1320–1325	0.61	0.44	0.37	1983-2004	1961-1982	0.50
1325–1500	0.65	0.44	0.36	1983-2004	1961-1982	0.53
1500–1520	0.64	0.45	0.37	1983-2004	1961-1982	0.55
1520–1725	0.66	0.49	0.42	1983-2004	1961-1982	0.59
1725–1750	0.65	0.47	0.40	1983-2004	1961-1982	0.58
1750–2006	0.67	0.48	0.42	1983-2004	1961-1982	0.60
2006–2010	0.71	0.50	0.44	1983-2004	1961-1982	0.61
2010–2013	0.72	0.45	0.39	1983-2004	1961-1982	0.58
2013–2016	0.71	0.42	0.35	1983-2004	1961-1982	0.54
2016–2018	0.70	0.37	0.29	1983-2004	1961-1982	0.49

Note: r^2 is is the regression R-squared for the model fit to the combined years of the split-sample calibration and validation periods.

Supplementary Table 3 Correlations of the original reconstructed streamflow with the AMV [16], PDO [17] and eastern Tibetan Plateau temperature reconstructions [18]. The data in brackets are the correlations of the reconstructed streamflow with AMV[16] and PDO[17] reconstructions after 30-yr smoothing.

Period	AMV	PDO	Tem.
1000–2018 CE	0.16 ** (0.45 **)	0.01 (-0.04)	0.49 ** (0.49**)
1050–1500 CE	0.37 ** (0.71 **)	-0.19 ** (-0.43 *)	0.38 ** (0.15)
1850–2018 CE	0.20 ** (0.77 **)	-0.11 (-0.43)	0.53** (0.77 **)

References

1. Chen, F. et al. 500-year tree-ring reconstruction of Salween River streamflow related to the history of water supply in Southeast Asia. *Clim*. *Dyn*. **53**, 6595-6607 (2019).

2. Chen, F. et al. Tree-ring reconstruction of Lhasa River streamflow reveals 472 years of hydrologic change on southern Tibetan Plateau. *J. Hydrol*. **572**, 169-178 (2019).

3. Nie, C. Y., Zhang, Q. B. & Lyu, L. Millennium-long tree-ring chronology reveals megadroughts on the southeastern Tibetan Plateau. *Tree Ring Res*. **73**, 1-10 (2017).

4. Holmes, R. L. Computer assisted quality control in tree-ring dating and measurement. *Tree Ring Bull*. **43**, 69-78 (1983).

5. Cook, E. R. & Kairiukstis, L. A. *Methods of dendrochronology: applications in the environmental sciences*. Kluwer Academic Publishers, Dordrecht, pp. 394 (1990).

6. Wigley, T. M., Briffa, K. R. & Jones, P. D. On the average value of correlated time series, with applications in dendroclimatology and hydrometeorology. *J. Appl*. *Meteorol*. *Climatol*. **23**, 201-213 (1984).

7. Meko, D. Dendroclimatic reconstruction with time varying predictor subsets of tree indices. *J. Clim*. **10**, 687-696 (1997).

8. Fritts, H. C. *Tree Rings and Climate* (Academic Press, 1976).

9. Otto-Bliesner, B. L. et al. Climate variability and change since 850 CE: An ensemble approach with the Community Earth System Model. *Bull*. *Am*. *Meteorol*. *Soc.* **97**, 735-754 (2016).

10. Ghiggi, G., Humphrey, V., Seneviratne, S. I. & Gudmundsson, L. G-RUN ENSEMBLE: A

Multi-Forcing Observation-Based Global Runoff Reanalysis. *Water Resour. Res.* **57**, e2020WR028787 (2021).

11. Hessl, A. E. et al. Past and future drought in Mongolia. *Sci. Adv.* **4**, e1701832 (2018).

12. Huang, X. et al. South Asian summer monsoon projections constrained by the interdecadal Pacific oscillation. *Sci. Adv.* **6**, eaay6546 (2020).

13. Sharmila, S., Joseph, S., Sahai, A. K., Abhilash, S. & Chattopadhyay, R. Future projection of Indian summer monsoon variability under climate change scenario: An assessment from CMIP5 climate models. *Glob. Planet. Change* **124**, 62-78 (2015).

14. Guo, L., Turner, A. G. & Highwood, E. J. Impacts of 20th century aerosol emissions on the South Asian monsoon in the CMIP5 models. *Atmospheric Chem. Phys.* **15**, 6367-6378 (2015).

15. Roxy, M. K., Ritika, K., Terray, P. & Masson, S. The curious case of Indian Ocean warming. *J. Clim.* **27**, 8501-8509 (2014).

16. Wang, J. et al. Internal and external forcing of multidecadal Atlantic climate variability over the past 1,200 years. *Nat. Geosci.* **10**, 512-517 (2017).

17. MacDonald, G. M. & Case, R. A. Variations in the Pacific Decadal Oscillation over the past millennium. *Geophys. Res. Lett.* **32**, L08703 (2005).

18. Wang, J., Yang, B. & Ljungqvist, F. C. A millennial summer temperature reconstruction for the eastern Tibetan Plateau from tree-ring width. *J. Clim.* **28**, 5289-5304 (2015).

19. Baran, E., Van Zalinge, N. & Bun, N. P. Floods, floodplains and fish production in the Mekong Basin: present and past trends. Proceedings of the Second Asian Wetlands Symposium, 27-30 August 2001, Penang, Malaysia. Penerbit Universiti Sains Malaysia, Pulau Pinang, Malaysia. 1116 pp (2001).